Applied Energy 364 (2024) 123104

Contents lists available at ScienceDirect

Applied Energy

journal homepage: www.elsevier.com/locate/apenergy

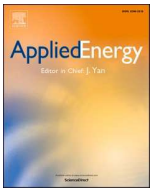

Impedance spectroscopy analysis of thermoelectric modules under actual energy harvesting operating conditions and a small temperature difference

Braulio Beltrán-Pitarch, Francisco Vidan, Marc Carbó, Jorge García-Cañadas *

Department of Industrial Systems Engineering and Design, Universitat Jaume I, Campus del Riu Sec, 12006 Castelló de la Plana, Spain

HIGHLIGHTS

- Equivalent circuits to use impedance spectroscopy under operating conditions.
- Constant temperature difference and constant heat power input modes analyzed.
- Main parameters can be obtained (module properties and thermal contact resistances).
- The origin of the processes that govern the I-V curve (power) can be identified.
- Powerful tool for in-situ characterization of devices and systems in applications.

ARTICLE INFO

Keywords:
Peltier device
Ac impedance
In-situ characterization
Constant temperature difference
Constant heat flux
Current-voltage curve

ABSTRACT

Thermoelectric (TE) devices can convert heat into electricity and have gained great interest as energy harvesters in many applications, such as self-powered sensors, solar TE generators and industrial waste heat recovery. Not many techniques are usually available for their characterization under operating conditions. Consequently, only current-voltage (power output) curves are typically reported to account for their performance, which provide limited information. Impedance spectroscopy, which has been mainly applied to the study of TE modules suspended in air or vacuum, has the advantage to be used under operating conditions. Here, we exploit this advantage and provide an in-depth analysis of the impedance response of standard TE devices when they operate under a small temperature difference. First, we derive the physical models (equivalent circuits) for the two most common operating conditions: (i) constant temperature difference and (ii) constant heat power input. Then, we use the obtained equivalent circuit to successfully fit experimental impedance measurements in both operating modes, which show significant differences. From the fittings, it is possible to obtain the thermal contact resistance between the TE device and the heat exchangers (heat source and heat sink) among other key parameters. In addition, we analyze the variations found in the impedance spectra for different current output levels. Moreover, we show how different electrical resistances, extracted from the impedance results, directly relate to the slope of the *I-V* curve (power output), and can provide very valuable information about the different processes that determine its value. All these results establish impedance spectroscopy as a very powerful tool to characterize TE devices under operating conditions and as a method that can provide highly valuable insights into their performance.

1. Introduction

Thermoelectric (TE) devices, also known as TE modules, are able to directly convert heat into electricity when they operate as energy harvesters, which have potential energy conversion applications ranging from industrial waste heat recovery to self-powered sensors [1,2]. In the energy harvesting operation mode, the device is subjected to a temperature difference. When this occurs, a voltage difference arises across the module at open circuit due to the Seebeck effect [1]. If the circuit is closed with a load, electrical current is produced.

The typical architecture of TE devices consists of a large number of TE legs which are electrically connected in series by metallic strips (usually copper) and thermally in parallel [1,3]. The TE legs are organized as an array of alternating n and p-type highly-doped

* Corresponding author.
E-mail address: garciaj@uji.es (J. García-Cañadas).

https://doi.org/10.1016/j.apenergy.2024.123104
Received 3 November 2023; Received in revised form 8 February 2024; Accepted 23 March 2024
Available online 6 April 2024

semiconductors, which are the TE materials. Electrically-insulating plates (usually alumina ceramics) are attached at the top and bottom sides of the TE legs structure and serve to establish the thermal contact with the heat sink and the heat source (or with the heat exchangers).

Impedance spectroscopy is a powerful characterization technique [4,5] that is widely used in many energy devices, such as Li-ion batteries, solar cells, fuel cells, etc. [6–8]. The method consists in applying a low amplitude sinusoidal current I_{ac} (or voltage) at a certain frequency f to the system. This ac perturbation oscillates around a fixed current (or voltage) level, usually known as the dc current I_{dc} (or dc voltage V_{dc}), and produces a sinusoidal potential difference variation V_{ac} (or current I_{ac}) in the system with the same frequency and at a certain phase shift (see Fig. 1). From this experiment, the impedance of the system Z at the given frequency is calculated from the voltage and current sinusoidal waves. The impedance value is represented in the complex plane (Nyquist plot) as a point which is defined by a vector whose angle is the phase shift angle ϕ and its module the voltage and current amplitudes ratio ($|Z| = V_{ac}/I_{ac}$), as shown in Fig. 1. This experiment is repeated in a wide range of frequencies (usually 1 MHz-10 mHz) and for each frequency a point is generated in the complex plane, creating the final impedance spectrum.

The fact of employing a wide range of frequencies typically allows the separation of the physical processes that occur in the device. At the highest frequencies, only the fastest processes can follow the quick perturbation. As the frequency decreases, processes that are slower progressively appear. This offers the possibility of having a kind of 'video' of the events happening in the system, due to the perturbation produced, as they evolve, which represents one of the main advantages of this method. In addition, powerful, accurate, and reliable instruments able to perform impedance experiments are available in the market and are frequently present in many research institutions. Another key advantage of the method is its capability to be applied under actual operating conditions.

Usually, experimental impedance results are analyzed by means of equivalent circuits (physical models), which represent the physical processes that occur in the system, such as electrical conduction, accumulation of charge, and diffusion phenomena, among others. The equivalent circuits are frequently formed by the combination of resistors, capacitors, inductors, Warburg elements, etc. [5,9]. From a fitting to the experimental impedance results using the equivalent circuit, highly valuable information of the system can be obtained. In many cases, more than one equivalent circuit can provide a good fitting to the experimental results. However, from all the possibilities, there is only one accounting for the actual physical phenomena. For this reason, it is very important to know the physics of the system, or perform further experiments to guarantee that the equivalent circuit employed is the correct one. This sometimes requires advanced expertise and represents one of the drawbacks of the method.

Impedance spectroscopy has been applied to the study of TE devices, mainly in the configuration when the device is suspended (neither in contact with a heat sink nor a heat source) [10–18] showing the possibility to obtain all the properties of the TE materials of the device. In addition, it has also been employed when a TE module is contacted by ideal heat sinks [19], showing the possibility to determine thermal contact resistances. However, a detailed impedance analysis of TE devices under actual energy harvesting operating conditions has not been performed yet. Under these conditions, a previous analysis [20] and some measurements have been reported [21,22]. However, these studies employed empirical and simplified models and did not analyze in detail the evolution of the impedance response at different current levels along the current-voltage (I-V) curve with accurate theoretical models, which should be obtained from the heat equation of the system.

In this work, we take advantage of the benefit of impedance spectroscopy to be used under operating conditions and provide an in-depth analysis of the impedance response of standard TE devices when they operate under actual energy harvesting conditions under a small temperature difference. In our analysis, we first derive the physical models (equivalent circuits) for two different conditions: (i) when the heat source of the system is kept at a constant temperature, and (ii) when the heat source provides a constant heat power input. These equivalent circuits are obtained by solving the heat equation of the system in the frequency domain. Then, we correlate the obtained theoretical models with experimental results, and show the significant differences that exist between the two conditions. Also, this correlation reveals the possibility to obtain the thermal contact resistance between the TE device and the heat exchangers (heat source and heat sink) among other key parameters. On the other hand, the variations found in the impedance response for different current output levels, and the contributions to the slope of the I-V curve, which governs the power output, from different electrical resistances extracted by the impedance analysis, are also analyzed.

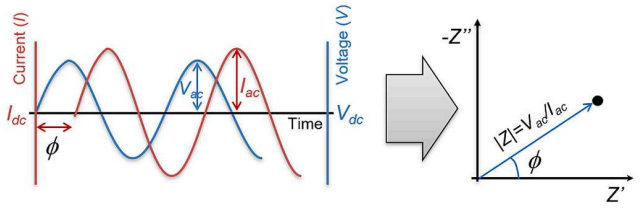

Fig. 1. Perturbation, system response and complex plane (Nyquist) representation of a single frequency point of an impedance spectroscopy experiment.

2. Theoretical models

The system under analysis comprises a TE device operating in the energy harvesting mode under a small temperature difference (e.g. 10 K). To establish the temperature difference, the device is thermally contacted at the hot side to a heat source (e.g. a copper block with inserted cartridge heaters) of the same area as the ceramic external layer of the TE device, and to a heat sink (e.g. a copper block with internal water circulation) at the cold side. It is assumed that thermal contact resistivities r_{TC} exist between the TE device and the heat source/heat sink, being both thermal contact resistivities identical (see Fig. 2).

The TE module consists of 2 N identical TE legs of cross-sectional area A and length L, being N the number of TE couples. The legs are

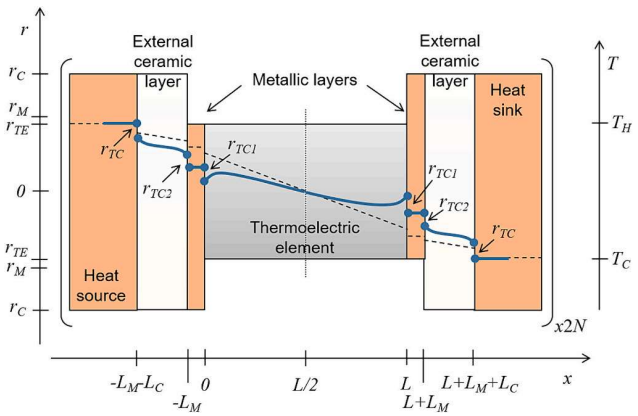

Fig. 2. Schematic view of the theoretical model considered for one of the legs that form a device with 2 N of these legs. The dashed line represents the initial temperature profile. The dotted line shows the plane where the temperature remains constant at all frequencies. The solid blue line represents a possible temperature profile when electrical current is generated. (For interpretation of the references to colour in this figure legend, the reader is referred to the web version of this article.)

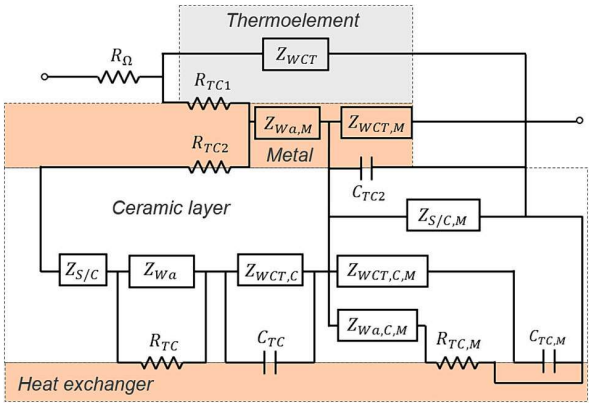

Fig. 3. Equivalent circuit for thermoelectric modules under actual constant temperature operating conditions and a small temperature difference.

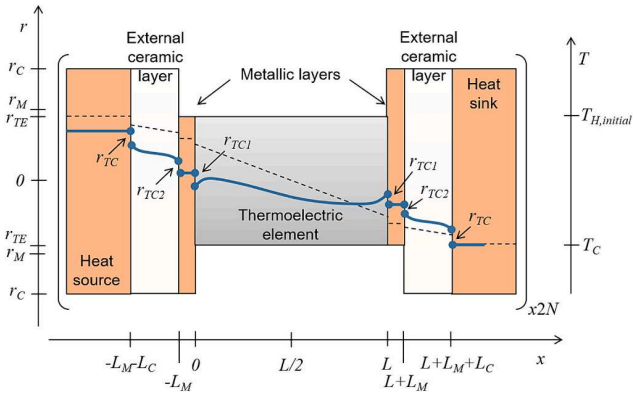

Fig. 4. Schematic view of the theoretical model considered for the constant heat power input case. One of the legs that form a device with 2 *N* of these legs is shown. The dashed line represents the initial temperature profile. The solid blue line represents a possible temperature profile when electrical current is generated. (For interpretation of the references to colour in this figure legend, the reader is referred to the web version of this article.)

contacted by two metallic strips (usually copper) with a slightly larger cross-sectional area A/η_M (being η_M the ratio between the area of all the TE legs and the area of all the metallic strips) and length L_M. Two external ceramic layers of cross-sectional area A/η (being η the filling factor of the TE module, i.e. the ratio between the area of all the TE legs and the ceramic area), and length L_C also form part of the device. At both sides of the metallic strips, the possibility of having a thermal contact resistance is considered, including r_{TC1} and r_{TC2} as thermal contact resistivities between the TE legs and metallic strips, and between the metallic strips and the ceramic layers, respectively (see Fig. 2).

Average and temperature independent materials properties are considered, being $S = |[S(x=0) + S(x=L)]/2|$, $\lambda_{TE} = [\lambda_{TE}(x=0) + \lambda_{TE}(x=L)]/2$, $\sigma = [\sigma(x=0) + \sigma(x=L)]/2$, and $\alpha_{TE} = [\alpha_{TE}(x=0) + \alpha_{TE}(x=L)]/2$ the average absolute Seebeck coefficient, average thermal conductivity, average electrical conductivity, and average thermal diffusivity of each of the identical TE legs that form the device. For the metallic strips, $\lambda_M = [\lambda_M(x=0) + \lambda_M(x=L)]/2$ and $\alpha_M = [\alpha_M(x=0) + \alpha_M(x=L)]/2$ are the average thermal conductivity and diffusivity. For the external ceramic layers, $\lambda_C = [\lambda_C(x=-L_M{-}L_C) + \lambda_C(x=L+L_M+L_C)]/2$ and $\alpha_C = [\alpha_C(x=-L_M{-}L_C) + \alpha_C(x=L+L_M+L_C)]/2$ are the average thermal conductivity and diffusivity. For the thermal contact resistivities, r_{TC}, r_{TC1}, and r_{TC2} are considered to be the average of the hot and cold sides values as well. It is also considered that the Peltier heat power at both junctions is equal to ST_MI, being $T_M = [T(x=0) + T(x=L)]/2$ and I the electrical current output.

In addition to the above description of the system under analysis, it is also assumed that Joule effect is neglected due to the high electrical conductivity of TE materials and the small current amplitude used during the impedance spectroscopy measurements. Finally, the system is also considered adiabatic (no radiation and convection losses).

The impedance function Z of a TE module with standard architecture (as described above in Fig. 2) is given by,

$$Z = \frac{V(L) - V(0)}{I_0} = j\omega L_p + R_\Omega - 2N\frac{S[\theta_L - \theta_0]}{i_0}, \tag{1}$$

where $V(0)$ and $V(L)$ are the voltages at $x=0$ and $x=L$, respectively, I_0 is the ac electrical current flowing through the device at $x=0$, $j = (-1)^{0.5}$ is the complex number, $\omega = 2\pi f$ the angular frequency, L_p the parasitic inductance, and R_Ω is the total ohmic resistance, which includes the contribution of all the TE legs of the TE module, the metallic strips, the leads, and the electrical contact resistances. Also, $\theta_x = \mathscr{L}[T(x) - T_{initial}(x)]$, indicating $\mathscr{L}$ the Laplace transform, and $i_0 = \mathscr{L}[I(0)]$.

In order to know θ_L and θ_0, the heat equation must be solved in the frequency domain for the system. At this point, it is important to differentiate between two different possible operation modes, which lead to different solutions of the heat equation (impedance functions): (i) constant temperature difference, or (ii) constant heat power input.

2.1. Constant temperature difference

This first case takes place when the temperature at the heat exchangers does not change during the entire impedance measurement. No temperature variation at the heat source, T_H, can occur when powering the cartridge heaters inserted in a copper block by a temperature controller, which powers the heaters of the heat source when a decrease in temperature is noticed in order to keep it constant. At the heat sink, no variation in temperature, T_C, can be produced by, for example, circulating water at a constant temperature through a copper block. It should be noticed that in this article T_H and T_C are the temperature of the heat source and heat sink, respectively, which are considered homogeneous within the heat source/sink material, and not the temperatures at the edges of the TE material. The configuration of the heat exchangers for this first case simulates an energy harvesting application of TE modules similar to the example of a hot exhaust gas circulating by a copper pipe. Being the hot side of the TE device in contact with the pipe, and with water circulation set at the cold side.

Fig. 2 represents this case, as it can be observed that the solid blue lines at the heat source and heat sink overlap with the initial temperature profile (dashed lines). The solution of the heat equation and the derivation of the impedance function for a system similar to this has already been developed by us in recent articles considering homogeneous initial temperature in the system [17,23]. From those articles, the equivalent circuit of Fig. 3 can be obtained when convection and radiation losses are discarded, and a prismatic geometry is considered.

In Fig. 3, the different elements of the equivalent circuit are defined as,

$$Z_{L_p} = j\omega L_p, \tag{2}$$

$$Z_{WCT} = \frac{2NS^2T_M L}{\lambda_{TE}A}\left(\frac{j\omega}{\omega_{TE}}\right)^{-0.5} tanh\left[\left(\frac{j\omega}{\omega_{TE}}\right)^{0.5}\right] = R_{TE}\left(\frac{j\omega}{\omega_{TE}}\right)^{-0.5} tanh\left[\left(\frac{j\omega}{\omega_{TE}}\right)^{0.5}\right], \quad (3)$$

$$\mathrm{R}_{TC1} = \frac{4NS^2T_M r_{TC1}}{A}, \quad (4)$$

$$Z_{Wa,M} = \frac{4NS^2T_M L_M \eta_M}{\lambda_M A}\left(\frac{j\omega}{\omega_M}\right)^{-0.5} coth\left[\left(\frac{j\omega}{\omega_M}\right)^{0.5}\right] = R_M\left(\frac{j\omega}{\omega_M}\right)^{-0.5} coth\left[\left(\frac{j\omega}{\omega_M}\right)^{0.5}\right], \quad (5)$$

$$Z_{WCT,M} = \frac{4NS^2T_M L_M \eta_M}{\lambda_M A}\left(\frac{j\omega}{\omega_M}\right)^{-0.5} tanh\left[\left(\frac{j\omega}{\omega_M}\right)^{0.5}\right] = R_M\left(\frac{j\omega}{\omega_M}\right)^{-0.5} tanh\left[\left(\frac{j\omega}{\omega_M}\right)^{0.5}\right], \quad (6)$$

$$R_{TC2} = \frac{4NS^2T_M r_{TC2}\eta_M}{A}, \quad (7)$$

$$Z_{S/C} = \frac{4NS^2T_M z_{s/c}\eta_M}{A}, \quad (8)$$

$$Z_{Wa} = \frac{4NS^2T_M L_C \eta}{\lambda_C A}\left(\frac{j\omega}{\omega_C}\right)^{-0.5} coth\left[\left(\frac{j\omega}{\omega_C}\right)^{0.5}\right] = R_C\left(\frac{j\omega}{\omega_C}\right)^{-0.5} coth\left[\left(\frac{j\omega}{\omega_C}\right)^{0.5}\right], \quad (9)$$

$$R_{TC} = \frac{4NS^2T_M r_{TC}\eta}{A}, \quad (10)$$

$$Z_{WCT,C} = \frac{4NS^2T_M L_C \eta}{\lambda_C A}\left(\frac{j\omega}{\omega_C}\right)^{-0.5} tanh\left[\left(\frac{j\omega}{\omega_C}\right)^{0.5}\right] = R_C\left(\frac{j\omega}{\omega_C}\right)^{-0.5} tanh\left[\left(\frac{j\omega}{\omega_C}\right)^{0.5}\right], \quad (11)$$

$$Z_{C_{TC}} = \frac{4NS^2T_M {L_C}^2 \eta}{{\lambda_C}^2 A r_{TC}}\left(\frac{j\omega}{\omega_C}\right)^{-1} = \frac{{R_C}^2}{R_{TC}}\left(\frac{j\omega}{\omega_C}\right)^{-1} = \frac{1}{j\omega C_{TC}}, \quad (12)$$

$$Z_{C_{TC2}} = \frac{4NS^2T_M {L_M}^2 \eta_M}{{\lambda_M}^2 A r_{TC2}}\left(\frac{j\omega}{\omega_M}\right)^{-1} = \frac{{R_M}^2}{R_{TC2}}\left(\frac{j\omega}{\omega_M}\right)^{-1} = \frac{1}{j\omega C_{TC2}}, \quad (13)$$

$$Z_{S/C,M} = \frac{4NS^2T_M {L_M}^2 \eta_M}{{\lambda_M}^2 A z_{s/c}}\left(\frac{j\omega}{\omega_M}\right)^{-1} = \frac{{R_M}^2}{Z_{S/C}}\left(\frac{j\omega}{\omega_M}\right)^{-1}, \quad (14)$$

$$Z_{WCT,C,M} = \frac{4NS^2T_M {L_M}^2 \lambda_C \omega_M {\eta_M}^2}{{\lambda_M}^2 A L_C \eta \omega_C}\left(\frac{j\omega}{\omega_C}\right)^{-0.5} tanh\left[\left(\frac{j\omega}{\omega_C}\right)^{0.5}\right] = \frac{{R_M}^2}{R_C}\left(\frac{\omega_M}{\omega_C}\right)\left(\frac{j\omega}{\omega_C}\right)^{-0.5} tanh\left[\left(\frac{j\omega}{\omega_C}\right)^{0.5}\right], \quad (15)$$

$$Z_{C_{TC,M}} = \frac{4NS^2T_M {L_M}^2 \eta_M{}^2}{{\lambda_M}^2 A \eta r_{TC}}\left(\frac{j\omega}{\omega_M}\right)^{-1} = \frac{{R_M}^2}{R_{TC}}\left(\frac{j\omega}{\omega_M}\right)^{-1} = \frac{1}{j\omega C_{TC,M}}, \quad (16)$$

$$Z_{Wa,C,M} = \frac{4NS^2T_M {L_M}^2 \lambda_C \omega_M {\eta_M}^2}{{\lambda_M}^2 A L_C \eta \omega_C}\left(\frac{j\omega}{\omega_C}\right)^{-0.5} coth\left[\left(\frac{j\omega}{\omega_C}\right)^{0.5}\right] = \frac{{R_M}^2}{R_C}\left(\frac{\omega_M}{\omega_C}\right)\left(\frac{j\omega}{\omega_C}\right)^{-0.5} coth\left[\left(\frac{j\omega}{\omega_C}\right)^{0.5}\right], \quad (17)$$

$$R_{TC,M} = \frac{4NS^2T_M {L_M}^2 {\lambda_C}^2 \omega_M {\eta_M}^2 r_{TC}}{{\lambda_M}^2 A {L_C}^2 \eta \omega_C} = \frac{{R_M}^2 R_{TC}}{{R_C}^2}\left(\frac{\omega_M}{\omega_C}\right), \quad (18)$$

being $\omega_{TE} = \alpha_{TE}/(L/2)^2$, $\omega_M = \alpha_M/L_M^2$, $\omega_C = \alpha_C/L_C^2$, and $z_{s/c}$ the spreading-constriction impedance [23],

$$z_{s/c} = \frac{2x_2y_1}{\lambda_C\pi^2x_1y_2}\sum_{n=1}^{\infty}\frac{sin^2(\alpha_n x_1)}{n^2\gamma_n}\left[\frac{\gamma_n\lambda_C r_{TC} + tanh(\gamma_n L_C)}{\gamma_n\lambda_C tanh(\gamma_n L_C) r_{TC} + 1}\right] + \frac{2y_2x_1}{\lambda_C\pi^2y_1x_2}\sum_{m=1}^{\infty}\frac{sin^2(\beta_m y_1)}{m^2\gamma_m}\left[\frac{\gamma_m\lambda_C r_{TC} + tanh(\gamma_m L_C)}{\gamma_m\lambda_C tanh(\gamma_m L_C) r_{TC} + 1}\right] + \frac{4x_2y_2}{\lambda_C\pi^4x_1y_1}\sum_{n,m=1}^{\infty}\frac{sin^2(\alpha_n x_1)sin^2(\beta_m y_1)}{n^2m^2\gamma_{n,m}}\left[\frac{\gamma_{n,m}\lambda_C r_{TC} + tanh(\gamma_{n,m}L_C)}{\gamma_{n,m}\lambda_C tanh(\gamma_{n,m}L_C) r_{TC} + 1}\right], \quad (19)$$

where the constants $\alpha_n = n\pi/x_2$, $\beta_m = m\pi/y_2$, $\gamma_n = (\alpha_n^2 + j\omega/\alpha_C)^{1/2}$, $\gamma_m = (\beta_m^2 + j\omega/\alpha_C)^{1/2}$, and $\gamma_{n,m} = (\alpha_n^2 + \beta_m^2 + j\omega/\alpha_C)^{1/2}$ define all the possible solutions for the values n and m. The geometrical parameters $x_1 = (A/\eta)^{1/2}/2 + A^{1/2}/2$, $x_2 = (A/\eta)^{1/2}$, $y_1 = A^{1/2}/2$, and $y_2 = (A/\eta)^{1/2}/2$, are defined in the supplementary information of Ref. [23]. At steady state, the spreading-constriction impedance becomes a resistance [23],

$$R_{S/C} = \frac{4NS^2T_M r_{s/c}\eta_M}{A}, \quad (20)$$

$$r_{s/c} = \frac{2{x_2}^2y_1}{\lambda_C\pi^3x_1y_2}\sum_{n=1}^{\infty}\frac{sin^2(\alpha_n x_1)}{n^3}\left[\frac{\alpha_n\lambda_C r_{TC} + tanh(\alpha_n L_C)}{\alpha_n\lambda_C tanh(\alpha_n L_C) r_{TC} + 1}\right] + \frac{2{y_2}^2x_1}{\lambda_C\pi^3y_1x_2}\sum_{m=1}^{\infty}\frac{sin^2(\beta_m y_1)}{m^3}\left[\frac{\beta_m\lambda_C r_{TC} + tanh(\beta_m L_C)}{\beta_m\lambda_C tanh(\beta_m L_C) r_{TC} + 1}\right] + \frac{4x_2y_2}{\lambda_C\pi^4x_1y_1}\sum_{n,m=1}^{\infty}\frac{sin^2(\alpha_n x_1)sin^2(\beta_m y_1)}{n^2m^2\delta_{n,m}}\left[\frac{\delta_{n,m}\lambda_C r_{TC} + tanh(\delta_{n,m}L_C)}{\delta_{n,m}\lambda_C tanh(\delta_{n,m}L_C) r_{TC} + 1}\right] \quad (21)$$

where $\delta_{n,m} = (\alpha_n^2 + \beta_m^2)^{1/2}$.

The constant temperature Warburg element Z_{WCT} refers to the diffusion of the Peltier heat towards the thermoelement. Similarly, the Warburg elements ($Z_{Wa,M}$ and $Z_{WCT,M}$ for the metallic strips, and Z_{Wa}, $Z_{WCT,C}$, $Z_{WCT,C,M}$ and $Z_{Wa,C,M}$ for the ceramics) appear due to the heat diffusion. The resistor R_{TC1} takes into account the thermal contact resistance between the TE legs and the metallic strips, while R_{TC2} and C_{TC2} only appear when there is a thermal contact resistance between the metallic strips and the ceramics, and relate to this thermal contact resistance and the temperature variation at this contact, respectively. The elements $Z_{S/C}$ and $Z_{S/C,M}$ consider the heat spreading/constriction due to the difference in area between the TE legs and the metallic strips, and between the metallic strips and the ceramics, respectively. Finally, the elements R_{TC}, C_{TC}, $R_{TC,M}$, and $C_{TC,M}$ come from the thermal contact resistance between the outer ceramic surfaces of the TE module and the heat exchangers, being again linked to the thermal contact resistance (resistances) and the temperature variation at this contact (capacitance).

Then, the impedance function is given by,

$$Z = Z_{L_p} + R_\Omega + \left\{ {Z_{WCT}}^{-1} + \left[R_{TC1} + \left({Z_{Wa,M}}^{-1} + {Z_{TOT1}}^{-1} \right)^{-1} + \left({Z_{WCT,M}}^{-1} + Z_{TOT2} \right)^{-1} \right]^{-1} \right\}^{-1}, \quad (22)$$

being Z_{TOT1} and Z_{TOT2},

$$Z_{TOT1} = R_{TC2} + Z_{S/C} + \left(Z_{Wa}{}^{-1} + R_{TC}{}^{-1}\right)^{-1} + \left(Z_{WCT,C}{}^{-1} + Z_{C_{TC}}{}^{-1}\right)^{-1}, \quad (23)$$

$$Z_{TOT2} = Z_{C_{TC2}}{}^{-1} + Z_{S/C,M}{}^{-1} + \left(Z_{WCT,C,M} + Z_{C_{TC,M}}\right)^{-1} + \left(Z_{Wa,C,M} + R_{TC,M}\right)^{-1}. \quad (24)$$

It should be noted that for this constant temperature different case, the dc resistance R_{dc} of the system, which is the steady-state value of the impedance function $Z(f \to 0)$, is given by,

$$Z(f \to 0) = R_{\Omega} + \left[R_{IE}{}^{-1} + \left(R_{TC1} + R_M + R_{TC2} + R_{S/C} + R_C + R_{IC}\right)^{-1}\right]^{-1}. \quad (25)$$

2.2. Constant heat power input

The other mode of operation (constant heat power input) results when the heater cartridges of the copper block at the heat source are powered using a fixed voltage and a fixed current. While this ensures a constant power input, the temperature of the copper block with the heaters inserted (T_H) can change during the impedance measurement (see Fig. 4), in contrast to the constant temperature difference case where it was constant. This configuration can occur for example in solar TE generators, where a TE device is in contact at the hot side with a solar absorber element which is radiated by a fixed radiation level. If at the cold side water circulation is used, T_C will not change.

To obtain the total impedance function in this case, we identify first the heat source and heat sink impedances, Z_{So} and Z_{Si}, respectively. Notice that when constant heat power input is used, the temperature in the heat source and at $L/2$ is not constant during the impedance measurement and the system loses the antisymmetric temperature profile (see Fig. 2 and Fig. 4).

To calculate the impedance of the heat source the thermal quadrupole method [24] is employed. This method consists in defining a matrix for each material layer (TE leg, metallic strip, or ceramic) and thermal interface. For example, when obtaining the impedance at the heat source side of the TE legs, six matrices of four elements are used to relate the complex temperature in the TE legs (at $x = 0$) and at the heat source. These matrices represent: (i) the thermal contact between TE legs and metallic strips (at $x = 0$), (ii) the metallic strips, (iii) the thermal contact and spreading-constriction between the metallic strips and the ceramics (at $x = -L_M$), (iv) the ceramic layer, (v) the thermal contact between ceramic layer and the heat source (at $x = -L_M - L_C$), and (vi) the heat source. The complex temperatures and heat fluxes are represented by two single-column matrices for a total of eight matrices,

$$\begin{bmatrix} \theta_0 \\ \phi_{0,So} \end{bmatrix} = \begin{bmatrix} 1 & \frac{r_{TC1}}{A} \\ 0 & 1 \end{bmatrix} \begin{bmatrix} \cosh\left(\sqrt{\frac{j\omega}{\omega_M}}\right) & \frac{L_M \eta_M \sinh\left(\sqrt{\frac{j\omega}{\omega_M}}\right)}{\lambda_M A \sqrt{\frac{j\omega}{\omega_M}}} \\ \frac{\lambda_M A}{L_M \eta_M}\sqrt{\frac{j\omega}{\omega_M}}\sinh\left(\sqrt{\frac{j\omega}{\omega_M}}\right) & \cosh\left(\sqrt{\frac{j\omega}{\omega_M}}\right) \end{bmatrix} \begin{bmatrix} 1 & \frac{(r_{TC2} + z_{s/c})\eta_M}{A} \\ 0 & 1 \end{bmatrix}$$

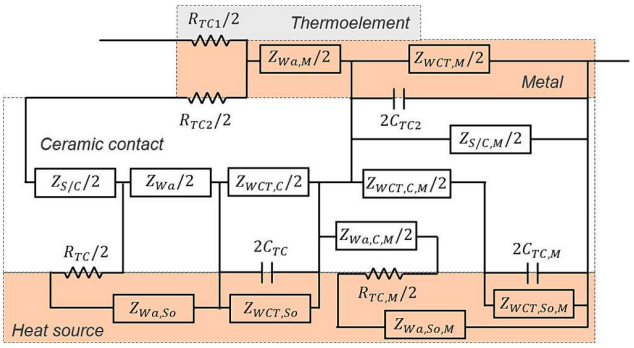

Fig. 5. Equivalent circuit that defines the heat source impedance (hot part of the thermoelectric module) under constant heat power input condition and a small temperature difference.

$$\begin{bmatrix} \cosh\left(\sqrt{\frac{j\omega}{\omega_C}}\right) & \frac{L_C \eta \sinh\left(\sqrt{\frac{j\omega}{\omega_C}}\right)}{\lambda_C A \sqrt{\frac{j\omega}{\omega_C}}} \\ \frac{\lambda_C A}{L_C \eta}\sqrt{\frac{j\omega}{\omega_C}}\sinh\left(\sqrt{\frac{j\omega}{\omega_C}}\right) & \cosh\left(\sqrt{\frac{j\omega}{\omega_C}}\right) \end{bmatrix} \begin{bmatrix} 1 & \frac{r_{TC}\eta}{A} \\ 0 & 1 \end{bmatrix}$$

$$\begin{bmatrix} \cosh\left(\sqrt{\frac{j\omega}{\omega_{So}}}\right) & \frac{L_{So} \eta \sinh\left(\sqrt{\frac{j\omega}{\omega_{So}}}\right)}{\lambda_{So} A \sqrt{\frac{j\omega}{\omega_{So}}}} \\ \frac{\lambda_{So} A}{L_{So} \eta}\sqrt{\frac{j\omega}{\omega_{So}}}\sinh\left(\sqrt{\frac{j\omega}{\omega_{So}}}\right) & \cosh\left(\sqrt{\frac{j\omega}{\omega_{So}}}\right) \end{bmatrix} \begin{bmatrix} \theta_{So} \\ 0 \end{bmatrix}. \quad (26)$$

After solving the quadrupole method, we reach the heat source impedance expression,

$$Z_{So} = \frac{\left[\frac{R_{TC1}}{2} + \left(\frac{2}{Z_{Wa,M}} + Z_{TOT3}{}^{-1}\right)^{-1} + \left(\frac{2}{Z_{WCT,M}} + \frac{2}{Z_{C_{TC2}}} + \frac{2}{Z_{S/C,M}} + Z_{TOT4}\right)^{-1}\right]}{2NS^2 T_M}, \quad (27)$$

where Z_{TOT3} and Z_{TOT4} are defined as,

$$Z_{TOT3} = \frac{R_{TC2}}{2} + \frac{Z_{S/C}}{2} + \left[\frac{2}{Z_{Wa}} + \left(\frac{R_{TC}}{2} + Z_{Wa,So}\right)^{-1}\right]^{-1} + \left(\frac{2}{Z_{WCT,C}} + \frac{2}{Z_{C_{TC}}} + Z_{WCT,So}{}^{-1}\right)^{-1}, \quad (28)$$

$$Z_{TOT4} = \left[\frac{Z_{WCT,C,M}}{2} + \left(\frac{2}{Z_{C_{TC,M}}} + \frac{2}{Z_{WCT,So,M}}\right)^{-1}\right]^{-1} + \left(\frac{Z_{Wa,C,M}}{2} + \frac{R_{TC,M}}{2} + Z_{Wa,So,M}\right)^{-1}. \quad (29)$$

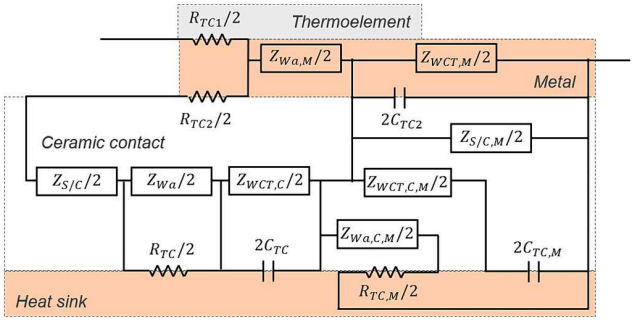

Fig. 6. Equivalent circuit that defines the heat sink impedance (cold part of the thermoelectric module) under constant heat power input condition and a small temperature difference.

From the derivation, different new elements of the equivalent circuit are found (see Fig. 5),

$$Z_{Wa,So} = \frac{2NS^2T_ML_{So}\eta}{\lambda_{So}A}\left(\frac{j\omega}{\omega_{So}}\right)^{-0.5} coth\left[\left(\frac{j\omega}{\omega_{So}}\right)^{0.5}\right] = R_{So}\left(\frac{j\omega}{\omega_{So}}\right)^{-0.5} coth\left[\left(\frac{j\omega}{\omega_{So}}\right)^{0.5}\right], \tag{30}$$

$$Z_{WCT,So} = \frac{2NS^2T_M{L_C}^2\lambda_{So}\omega_C\eta^2}{{\lambda_C}^2AL_{So}\omega_{So}}\left(\frac{j\omega}{\omega_{So}}\right)^{-0.5} tanh\left[\left(\frac{j\omega}{\omega_{So}}\right)^{0.5}\right] = \frac{{R_C}^2}{4R_{So}}\left(\frac{\omega_C}{\omega_{So}}\right)\left(\frac{j\omega}{\omega_{So}}\right)^{-0.5} tanh\left[\left(\frac{j\omega}{\omega_{So}}\right)^{0.5}\right], \tag{31}$$

$$Z_{WCT,So,M} = \frac{2NS^2T_M{L_M}^2\lambda_{So}\omega_M{\eta_M}^2}{{\lambda_M}^2A\eta L_{So}\omega_{So}}\left(\frac{j\omega}{\omega_{So}}\right)^{-0.5} tanh\left[\left(\frac{j\omega}{\omega_{So}}\right)^{0.5}\right] = \frac{{R_M}^2}{4R_{So}}\left(\frac{\omega_M}{\omega_{So}}\right)\left(\frac{j\omega}{\omega_{So}}\right)^{-0.5} tanh\left[\left(\frac{j\omega}{\omega_{So}}\right)^{0.5}\right], \tag{32}$$

$$Z_{Wa,So,M} = \frac{2NS^2T_M{L_M}^2{L_{So}}{\lambda_C}^2\omega_M{\eta_M}^2}{{\lambda_M}^2A\eta{L_C}^2\lambda_{So}\omega_C}\left(\frac{j\omega}{\omega_{So}}\right)^{-0.5} coth\left[\left(\frac{j\omega}{\omega_{So}}\right)^{0.5}\right] = \frac{{R_M}^2R_{So}}{{R_C}^2}\left(\frac{\omega_M}{\omega_C}\right)\left(\frac{j\omega}{\omega_{So}}\right)^{-0.5} coth\left[\left(\frac{j\omega}{\omega_{So}}\right)^{0.5}\right], \tag{33}$$

being L_{So}, λ_{So}, and α_{So} the length, thermal conductivity, and the thermal diffusivity of the heat source, which also define $\omega_{So} = \alpha_{So}/L_{So}^2$. The four Warburg elements are the consequence of the heat diffusion in the heat source.

To calculate the impedance of the heat sink Z_{Si}, the thermal quadrupole method is also used,

$$\begin{bmatrix}\theta_L\\ \phi_{L,Si}\end{bmatrix} = \begin{bmatrix}1 & \frac{r_{TC1}}{A}\\ 0 & 1\end{bmatrix}\begin{bmatrix} cosh\left(\sqrt{\frac{j\omega}{\omega_M}}\right) & \frac{L_M\eta_M sinh\left(\sqrt{\frac{j\omega}{\omega_M}}\right)}{\lambda_M A\sqrt{\frac{j\omega}{\omega_M}}}\\ \frac{\lambda_M A}{L_M\eta_M}\sqrt{\frac{j\omega}{\omega_M}}sinh\left(\sqrt{\frac{j\omega}{\omega_M}}\right) & cosh\left(\sqrt{\frac{j\omega}{\omega_M}}\right)\end{bmatrix}\begin{bmatrix}1 & \frac{(r_{TC2}+z_{s/c})\eta_M}{A}\\ 0 & 1\end{bmatrix}$$

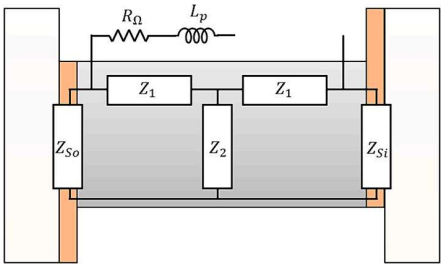

Fig. 7. Equivalent circuit for thermoelectric modules under actual constant temperature operating conditions and a small temperature difference. Notice that the impedance element Z_{So} represents the 19 elements shown in Fig. 5 and Z_{Si} contains the 15 elements of Fig. 6. The impedance elements Z_1 and Z_2 account for the heat transport in the thermoelectric legs.

Table 1
Properties of the thermoelectric device tested.

Size (mm^2)	N	L (mm)	L_M (mm)	L_C (mm)	A (mm^2)	η_M	η
40 × 40	127	1.06	0.22	0.74	1.34 × 1.34	0.67	0.27

$$\begin{bmatrix} cosh\left(\sqrt{\frac{j\omega}{\omega_C}}\right) & \frac{L_C\eta sinh\left(\sqrt{\frac{j\omega}{\omega_C}}\right)}{\lambda_C A\sqrt{\frac{j\omega}{\omega_C}}}\\ \frac{\lambda_C A}{L_C\eta}\sqrt{\frac{j\omega}{\omega_C}}sinh\left(\sqrt{\frac{j\omega}{\omega_C}}\right) & cosh\left(\sqrt{\frac{j\omega}{\omega_C}}\right)\end{bmatrix}\begin{bmatrix}\theta_{Si}\\ \frac{A}{\eta r_{TC}}\theta_{Si}\end{bmatrix}. \tag{34}$$

After solving the quadrupole method, the heat sink impedance expression, represented by the equivalent circuit of Fig. 6 is obtained,

$$Z_{Si} = \frac{\left[\frac{R_{TC1}}{2} + \left(\frac{2}{Z_{Wa,M}} + {Z_{TOT5}}^{-1}\right)^{-1} + \left(\frac{2}{Z_{WCT,M}} + Z_{TOT6}\right)^{-1}\right]}{2NS^2T_M}, \tag{35}$$

where Z_{TOT5} and Z_{TOT6} are defined as,

$$Z_{TOT5} = \frac{R_{TC2}}{2} + \frac{Z_{S/C}}{2} + \left(\frac{2}{Z_{Wa}} + \frac{2}{R_{TC}}\right)^{-1} + \left(\frac{2}{Z_{WCT,C}} + \frac{2}{Z_{C_{TC}}}\right)^{-1}, \tag{36}$$

$$Z_{TOT6} = \frac{2}{Z_{C_{TC2}}} + \frac{2}{Z_{S/C,M}} + \left(\frac{Z_{WCT,C,M}}{2} + \frac{Z_{C_{TC,M}}}{2}\right)^{-1} + \left(\frac{Z_{Wa,C,M}}{2} + \frac{R_{TC,M}}{2}\right)^{-1}. \tag{37}$$

To reach the total impedance of the system, the effect of the TE legs should be added to the heat source and heat sink impedances, so the thermal quadrupole method is again used for this purpose,

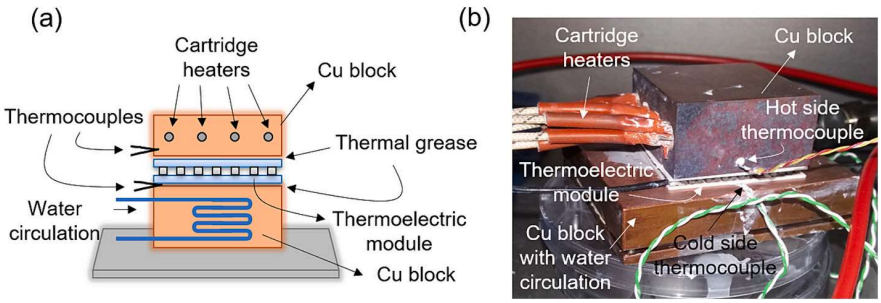

Fig. 8. (a) Schematic and (b) picture of the setup employed to measure the thermoelectric device under energy generation mode.

$$\begin{bmatrix} \theta_0 \\ \phi_0 - \dfrac{\theta_0}{Z_{So}} \end{bmatrix} = \begin{bmatrix} cosh\left(\sqrt{\dfrac{j\omega}{\omega_{TE2}}}\right) & \dfrac{Lsinh\left(\sqrt{\dfrac{j\omega}{\omega_{TE2}}}\right)}{\lambda_{TE}A\sqrt{\dfrac{j\omega}{\omega_{TE2}}}} \\ \dfrac{\lambda_{TE}A}{L}\sqrt{\dfrac{j\omega}{\omega_{TE2}}}sinh\left(\sqrt{\dfrac{j\omega}{\omega_{TE2}}}\right) & cosh\left(\sqrt{\dfrac{j\omega}{\omega_{TE2}}}\right) \end{bmatrix} \begin{bmatrix} \theta_L \\ \phi_L + \dfrac{\theta_L}{Z_{Si}} \end{bmatrix}, \tag{38}$$

being now $\omega_{TE2} = \alpha_{TE}/L^2$. However, the solution cannot be computed, and it is necessary to define the quadrupole with exponentials [25],

$$\begin{bmatrix} \dfrac{\theta_0}{e^{\sqrt{\frac{j\omega}{\omega_{TE2}}}}} \\ \phi_0 - \dfrac{\theta_0}{Z_{So}} \\ \hline e^{\sqrt{\frac{j\omega}{\omega_{TE2}}}} \end{bmatrix} = \begin{bmatrix} \dfrac{1+e^{-2\sqrt{\frac{j\omega}{\omega_{TE2}}}}}{2} & \dfrac{L\left(1-e^{-2\sqrt{\frac{j\omega}{\omega_{TE2}}}}\right)}{2\lambda_{TE}A\sqrt{\dfrac{j\omega}{\omega_{TE2}}}} \\ \dfrac{\lambda_{TE}A}{2L}\sqrt{\dfrac{j\omega}{\omega_{TE2}}}\left(1-e^{-2\sqrt{\frac{j\omega}{\omega_{TE2}}}}\right) & \dfrac{1+e^{-2\sqrt{\frac{j\omega}{\omega_{TE2}}}}}{2} \end{bmatrix} \begin{bmatrix} \theta_L \\ \phi_L + \dfrac{\theta_L}{Z_{Si}} \end{bmatrix}. \tag{39}$$

After some algebraic steps, θ_0 and θ_l can be obtained,

$$\theta_0 = \frac{\frac{\phi_0+\phi_0 e^{-2\sqrt{\frac{j\omega}{\omega_{TE2}}}}}{2} + \frac{\phi_0 L\left(1-e^{-2\sqrt{\frac{j\omega}{\omega_{TE2}}}}\right)}{Z_{Si}2\lambda_{TE}A\sqrt{\frac{j\omega}{\omega_{TE2}}}} - \phi_L e^{-\sqrt{\frac{j\omega}{\omega_{TE2}}}}}{\frac{\lambda_{TE}A}{2L}\sqrt{\frac{j\omega}{\omega_{TE2}}}\left(1-e^{-2\sqrt{\frac{j\omega}{\omega_{TE2}}}}\right) + \frac{1+e^{-2\sqrt{\frac{j\omega}{\omega_{TE2}}}}}{2Z_{Si}} + \frac{1+e^{-2\sqrt{\frac{j\omega}{\omega_{TE2}}}}}{2Z_{So}} + \frac{L\left(1-e^{-2\sqrt{\frac{j\omega}{\omega_{TE2}}}}\right)}{2Z_{Si}Z_{So}\lambda_{TE}A\sqrt{\frac{j\omega}{\omega_{TE2}}}}}, \tag{40}$$

$$\theta_L = \frac{\phi_0 e^{-\sqrt{\frac{j\omega}{\omega_{TE2}}}} - \frac{\theta_0 e^{-\sqrt{\frac{j\omega}{\omega_{TE2}}}}}{Z_{So}} - \frac{\phi_L+\phi_L e^{-2\sqrt{\frac{j\omega}{\omega_{TE2}}}}}{2}}{\frac{\lambda_{TE}A}{2L}\sqrt{\frac{j\omega}{\omega_{TE2}}}\left(1-e^{-2\sqrt{\frac{j\omega}{\omega_{TE2}}}}\right) + \frac{1+e^{-2\sqrt{\frac{j\omega}{\omega_{TE2}}}}}{2Z_{Si}}}. \tag{41}$$

Finally, the total impedance under constant heat power, $Z = V/I$ is given by Eq. (1) when Eq. (40) and Eq. (41) are introduced. The final equivalent circuit that fully describes the constant heat power condition is represented in Fig. 7, where the elements Z_1, and Z_2, are,

$$Z_1 = \frac{cosh\left(\sqrt{\frac{j\omega}{\omega_{TE2}}}\right) - 1}{\frac{\lambda_{TE}A}{L}\sqrt{\frac{j\omega}{\omega_{TE2}}}sinh\left(\sqrt{\frac{j\omega}{\omega_{TE2}}}\right)}, \tag{42}$$

$$Z_2 = \frac{1}{\frac{\lambda_{TE}A}{L}\sqrt{\frac{j\omega}{\omega_{TE2}}}sinh\left(\sqrt{\frac{j\omega}{\omega_{TE2}}}\right)}, \tag{43}$$

It should be noted that for this constant heat power input case, the dc resistance of the system is given by,

$$Z(f \to 0) = R_\Omega + R_{TE}. \tag{44}$$

Table 2
Temperature values for the impedance measurements obtained under constant heat power input for different dc currents.

I_{dc} (A)	T_H (°C)	T_C (°C)	ΔT (K)	T_M (°C)
0	25.0	15.0	10.0	20.0
−0.07	24.0	15.0	9.0	19.5
−0.14	22.4	15.0	7.4	18.7
−0.18	21.6	15.0	6.6	18.3

3. Experimental part

In order to validate the equivalent circuits developed, impedance measurements were performed using a standard Bi_2Te_3 TE device from European Thermodynamics (ref. GM250-127-14-10) with the properties shown in Table 1. The module was attached at the cold side to a copper block with water circulation (see Fig. 8). The water was circulated using a thermostatic circulating bath (PolyScience, SD07R-20-A12E). A copper block (40 mm × 40 mm × 20 mm) with 4 cartridge heaters (Watlow, ref. E1J49-L12) inserted was used as the heat source. When experiments under constant temperature difference were run, the heaters were powered by a temperature controller (Watlow, EZ-Zone PM). In the case of experiments under a constant heat power input, the heaters were powered at a constant current and voltage values using a variable transformer (RS, ref. 890-2872). A thin layer of a thermal interface material (thermal grease from RS, ref. 217-3835) was placed at the two interfaces of the TE module with the heat source and heat sink. The hot and cold side temperatures were measured using K-type thermocouples (RS, ref. 363-0250). At the hot side, the thermocouple was place inside a small hole machined in the copper block, which was filled with thermal grease to improve the thermal contact (see Fig. 8). At the cold side, the thermocouple was located in a groove machined on the copper block, which was also filled with thermal grease (see Fig. 8).

Before mounting the device in the setup of Fig. 8, it was measured under suspended conditions in vacuum (pressure $< 1.0 \times 10^{-4}$ mbar) inside a metallic vacuum chamber, which also acted as a Faraday cage. Under suspended conditions, an impedance measurement was performed at a 20.0 °C ambient temperature using a 50 mA ac current oscillating around a 0 A dc value and employing a frequency range from 10 mHz to 100 kHz, measuring in total 40 points logarithmically distributed. After the impedance measurement, the Seebeck coefficient was measured by applying different constant currents (50, 100, 150, and 200 mA) to the suspended module in vacuum. Once steady state is achieved after applying each current value (a temperature difference

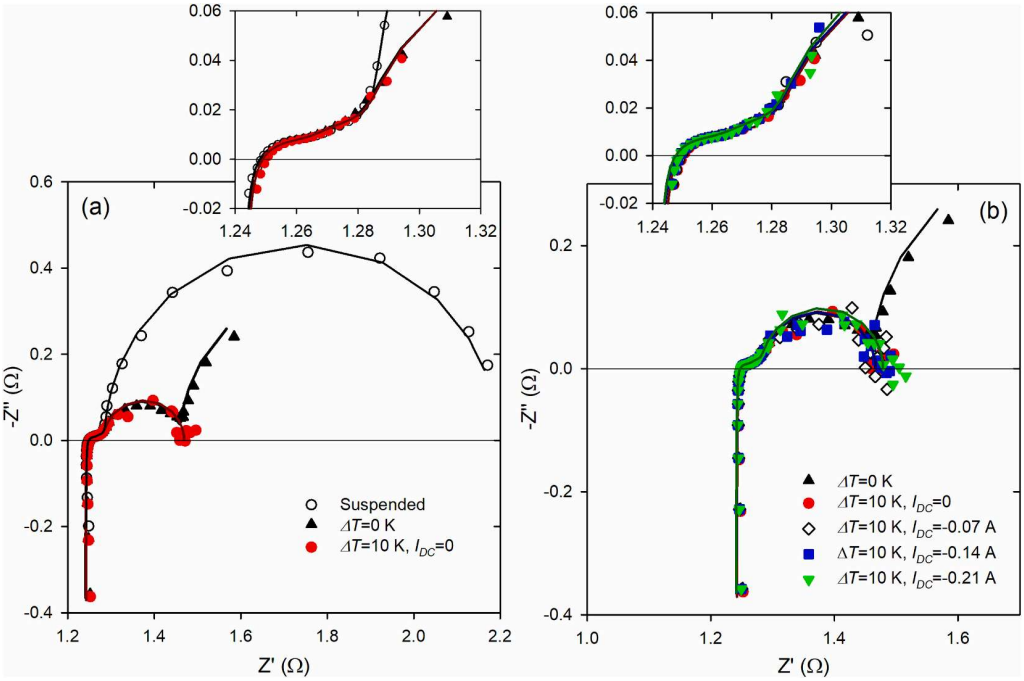

Fig. 9. Experimental impedance measurements (points) and their corresponding fittings (lines) for different conditions. (a) Impedance response of the module suspended in vacuum, sandwiched between the heat exchangers under no temperature difference ($I_{DC} = 0$), and under 10 K temperature difference for the constant temperature difference condition. (b) Impedance response of the module sandwiched between the heat exchangers under no temperature difference, and under a 10 K temperature difference under constant temperature condition at different dc currents. The insets represent magnifications of zones of interest.

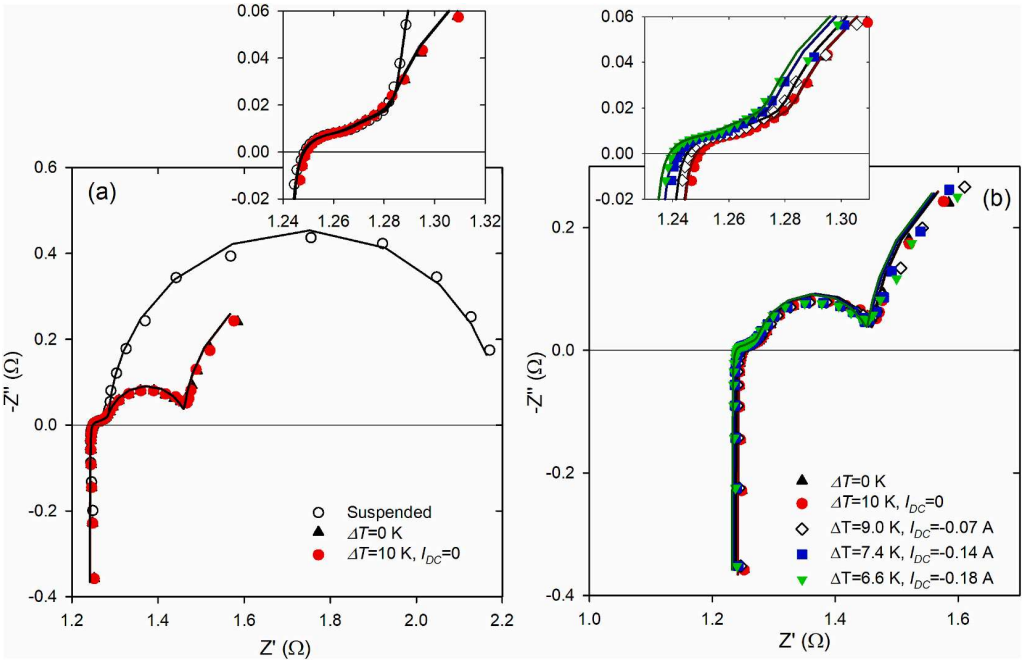

Fig. 10. Experimental impedance measurements (points) and their corresponding fittings (lines) for different conditions. (a) Impedance response of the module suspended in vacuum, sandwiched between the heat exchangers under no temperature difference, and under 10 K temperature difference for the constant heat power input condition. (b) Impedance response of the module sandwiched between the heat exchangers under no temperature difference, and at an initial 10 K temperature difference under constant heat power condition at different dc currents. The insets represent magnifications of zones of interest.

appears that is due to the Peltier effect), the circuit was opened and the voltage and the temperature difference between the outer layers were measured immediately. The temperature difference was measured with the same K-type thermocouples touching the central part of the outer layers and using a bit of thermal grease at their tips. The absolute Seebeck coefficient value (205.8 μV/K) was obtained from the slope of the voltage vs temperature difference plot.

After these measurements, the device was assembled in the setup of

Table 3
Fitting parameters with their associated relative errors (in brackets) of the impedance spectra of Fig. 9 and Fig. 10, performed at different conditions.

	L_p (H)	R_Ω (Ω)	r_{TC1} (m^2KW^{-1})	λ_{TE} ($Wm^{-1}K^{-1}$)	λ_C ($Wm^{-1}K^{-1}$)	r_{TC} (m^2KW^{-1})
Suspended	3.24×10^{-7} (1.41%)	1.242 (0.032%)	1.01×10^{-5} (3.07%)	1.96 (0.56%)	30.29 (0.84%)	–
Sandwiched	5.83×10^{-7} (2.15%)	1.241 (0.054%)	–	–	–	2.23×10^{-4} (2.29%)
ΔT constant 0 A	5.92×10^{-7} (3.12%)	1.241 (0.077%)	–	–	–	2.37×10^{-4} (2.69%)
ΔT constant −0.07 A	5.80×10^{-7} (4.48%)	1.240 (0.099%)	–	–	–	2.33×10^{-4} (3.53%)
ΔT constant −0.14 A	5.81×10^{-7} (4.43%)	1.240 (0.101%)	–	–	–	2.34×10^{-4} (3.59%)
ΔT constant −0.21 A	5.81×10^{-7} (4.30%)	1.240 (0.101%)	–	–	–	2.57×10^{-4} (3.49%)
Q_{in} constant 0 A	5.83×10^{-7} (2.15%)	1.241 (0.051%)	–	–	–	2.24×10^{-4} (2.18%)
Q_{in} constant −0.07 A	5.71×10^{-7} (3.86%)	1.237 (0.083%)	–	–	–	2.30×10^{-4} (3.51%)
Q_{in} constant −0.14 A	5.70×10^{-7} (3.63%)	1.234 (0.077%)	–	–	–	2.29×10^{-4} (3.36%)
Q_{in} constant −0.18 A	5.71×10^{-7} (3.38%)	1.231 (0.075%)	–	–	–	2.27×10^{-4} (3.17%)

Fig. 8 and several impedance measurements were performed employing the same parameters of the suspended module measurement, except the frequency range (2 mHz to 100 kHz was used). First, an impedance was obtained with only water circulation at the heat sink, being for this case the initial hot and cold side temperatures $T_H = T_C = 20.0$ °C ($\Delta T = 0.0$ K). Then, impedance measurements were carried out under constant temperature difference. The hot and cold side temperatures were fixed to 25.0 and 15.0 °C, respectively ($\Delta T = 10.0$ K and $T_M = 20.0$ °C). Under these conditions, impedances (using 50 mA ac current) were performed at 0, −0.07, −0.14, and −0.21 A dc currents, waiting 20 min between each measurement to ensure reaching the steady state. Finally, impedance measurements (using 50 mA ac current) were performed under constant heat power input at 0, −0.07, −0.14, and −0.18 A dc currents, waiting 20 min between each measurement to ensure reaching the steady state as well. All the temperature values for the constant heat power input experiments are shown in Table 2. In this case, in contrast with the constant temperature difference regime, the hot side temperature changes when current flows due to the Peltier effect (the TE device is a refrigerator), and hence the average temperature T_M.

It should be mentioned that at each I_{dc} value, the dc voltage V_{dc} was also recorded for the impedance experiments of the constant temperature difference, and constant heat power input systems, in order to plot their *I-V* characteristics. In addition, the *I-V* curve for the suspended in vacuum system was also recorded for comparison, applying different fixed current values (0.05, 0.1, 0.15, and 0.2 A) and registering the corresponding voltage after reaching steady state. Moreover, a fast *I-V* curve, performed at a 100 V/s scan rate, was carried out to the system under the constant temperature difference of 10.0 K ($T_H = 25.0$ °C, $T_C = 15.0$ °C). At such a high scan rate the temperature profile of the system is not expected to change. All the impedance experiments and the electrical signals were recorded using a Metrohm Autolab Vionic instrument, controlled by Intello 1.2 software.

4. Results and discussion

All the impedance spectroscopy results with their fittings can be seen in Fig. 9 and Fig. 10. In addition, Table 3 shows all the fitted parameters and their associated relative errors, provided by the fitting. The impedance response when the module was suspended in vacuum is shown both in Fig. 9a and Fig. 10a. The fitting to this measurement provides all the module properties which will be kept fixed in the rest of the fittings, since they do not vary. In order to perform the fitting of the suspended module, a simplified version of the equivalent circuit of Fig. 3 that considers $r_{TC} \to \infty$ was used, which is the same equivalent circuit described in Ref. [23]. For this purpose, we used the MATLAB code provided in Ref. [23]. As explained in that article, first, the specifications of the TE module (see Table 1) are provided to the code. Then, we choose L_p, R_Ω, r_{TC1}, λ_{TE}, and λ_C as the parameters to fit, and maintain fixed the values of $S = 205.8$ μV/K (experimentally determined as mentioned above), $T_M = 20.0$ °C (the initial uniform temperature of the device), $\alpha_{TE} = 0.37$ mm^2s^{-1}, $\alpha_C = 10$ mm^2s^{-1}, $\lambda_M = 400$ $Wm^{-1}K^{-1}$, $\alpha_M = 110$ mm^2s^{-1}, and $r_{TC2} = 0$. As discussed in Ref. [17], the value of r_{TC2} is usually very low, since the metal strips/outer ceramic layers thermal contacts are really good, and thus it can be neglected. In the same reference, the values of α_{TE}, α_C, λ_M, and α_M were set as constants since impedance measurements are less sensitive to them. As it can be seen in Fig. 9a and Fig. 10a, the fitting performed to the suspended module excellently fits to the experimental results, and provides the module properties (L_p, R_Ω, r_{TC1}, λ_{TE}, and λ_C) with low relative errors. All fittings were performed using the MATLAB function *lsqnonlin* (non-linear least square method) and the errors were calculated from the variance-covariance matrix. These values will be fixed in the rest of the fittings to be performed.

We now analyze first the impedance results for the case under constant temperature difference. When the system is under $\Delta T = 10$ K and the impedance measurement is performed at $I_{dc} = 0$ A, the response

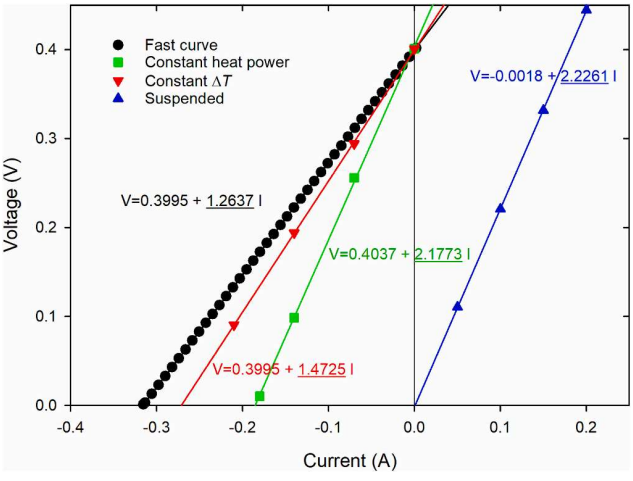

Fig. 11. Current-voltage characteristics of the different systems analyzed. Lines indicate the linear fits, and their equations are included. The underlined values in the equations are the resistances ($R_{I\text{-}V}$).

Table 4
Different resistances obtained from the impedance measurements that contribute to the total resistance (R_{dc}) and its comparison with the resistances from the *I-V* curves. For the fast curve case, R_{dc} corresponds to the R_{Ω} value from the suspended impedance measurement.

	R_{Ω} (Ω)	R_{TE} (Ω)	$R_{S/C}$ (Ω)	R_{TC} (Ω)	R_{TC1} (Ω)	R_C (Ω)	R_M (Ω)	R_{dc} (Ω)	$R_{I\text{-}V}$ (Ω)	Deviation (%)
Fast curve	–	–	–	–	–	–	–	1.242	1.264	1.77
Constant heat power	1.241	0.949	1.87×10^{-2}	0.212	3.55×10^{-2}	2.32×10^{-2}	1.29×10^{-3}	2.190	2.177	−0.59
Constant ΔT	1.241	0.949	1.87×10^{-2}	0.225	3.55×10^{-2}	2.32×10^{-2}	1.29×10^{-3}	1.471	1.473	0.14
Suspended	1.242	0.949	1.91×10^{-2}	–	3.55×10^{-2}	2.32×10^{-2}	1.29×10^{-3}	2.191	2.226	1.60

overlaps with the suspended module at frequencies >10 Hz, approximately (inset of Fig. 9a), but when the frequency decreases, a much smaller semicircle is observed (full red dots of Fig. 9). The overlapped region corresponds to the processes that occur in both systems until the moment when the injected Peltier fluxes at the metal/thermoelements junctions reach the outer faces of the external ceramic layers of the module. These processes are the same for both cases, since the differences only appear when the heat fluxes sense the heat exchangers and cross the thermal contact (r_{TC}). The strong reduction of the semicircle is due to the constant temperature condition, which removes the heat reaching the copper block at the cold side and does not let the temperature change at the copper block that acts as the heat source. Hence, the final temperature difference (T_H-T_C) will not increase, in contrast to the suspended case, where the heat is stored/removed in the ceramic layers instead of being extracted or cancelled by the heat exchangers, producing a larger temperature difference in the device, and hence a larger semicircle. As we reported in Ref. [19], the semicircle observed under constant temperature conditions strongly depends on the module/heat exchangers thermal contact, and decreases significantly when r_{TC} is reduced. The fitting performed to the system under $\Delta T = 10$ K was carried out using the equivalent circuit of Fig. 3, obtaining again an excellent agreement with the experimental results. From the fitting, L_p, R_{Ω} and r_{TC} were determined (see Table 3).

It can be also observed in Fig. 9a that the impedance response of the system under $\Delta T = 10$ K overlaps for most of the frequencies with the system when $\Delta T = 0$ K. Differences only occur at the lowest frequencies, where the $\Delta T = 0$ K system (sandwiched device) exhibits a vertical rise (onset of a semicircle), due to the fact that the temperature controller is turned off at the heat source and the copper block is allowed to change its temperature. Fig. 9b shows the variation of the impedance response when the system under a fixed $\Delta T = 10$ K was evaluated at different dc current values of the *I-V* curve. It can be observed that all the spectra basically overlap, as expected, since the average temperature does not change and the TE properties do not vary significantly with temperature due to the small temperature gradient. Fittings again agree well with experiments and similar values of the fitted parameters result (see Table 3).

We analyze now the impedance results for the case of constant heat power input. Fig. 10a shows the difference between the suspended system and the case when $\Delta T = 10$ K and the heat power input is fixed (at $I_{DC} = 0$). The response of the latter completely overlaps with the case when no input heat power is present (triangles in Fig. 10a) and hence $\Delta T = 0$ K (sandwiched system), also shown in Fig. 10a. This is expected, since the average temperature is identical in both cases and the TE properties do not vary significantly with temperature. As mentioned before, it can be observed that the main difference between the constant heat power input and the constant temperature difference systems is the existence of an onset of a semicircle for the former. This semicircle would continue until closing at the same values than the suspended measurement if lower frequencies had been registered, as predicted by Eq. (25). However, this was not possible experimentally since it would lead to an extremely lengthy measurement, since the dynamics of the system are slow. The fittings to the sandwiched ($\Delta T = 0$ K) and $\Delta T = 10$ K with fixed heat power input systems were performed using the equivalent circuit of Fig. 7, employing the MATLAB code in the Supplementary Information. From the fitting, L_p, R_{Ω} and r_{TC} were obtained (see Table 3).

Fig. 10b shows the impedance spectra of the system under a fixed heat power input at different dc current values along the *I-V* curve. It can be observed that all of them basically overlap, as in the constant temperature difference case, however, as shown in the inset of the figure, the value of the intercept with the real axis (ohmic resitance) slightly varies, adopting lower values when the I_{dc} increases. This occurs since the temperature difference is no longer constant, due to the absence of a temperature controller (constant temperature difference condition), and decreases with the dc current. Thus, the average temperature decreases, producing the observed variation in the ohmic resistance, which is the trend taking place in commercial modules when the temperature changes [14]. This was not the case in Fig. 9b (constant temperature difference) where the average temperature was always constant. Fittings again agree well with experiments and similar values of the fitted parameters are found (see Table 3).

The different *I-V* curves recorded for the systems analyzed are shown in Fig. 11. All of them show a linear trend and were fitted using the equations shown in the figure. The slopes of the curves, underlined in the figure, are the resistances given by the *I-V* curves ($R_{I\text{-}V}$), which are significantly different for the cases of constant temperature difference and constant heat power input. For this reason, it is important to indicate the method employed when the *I-V* characteristics of TE modules are determined. A higher power output is always expected for the constant temperature difference case. It should be noted that the values of $R_{I\text{-}V}$ agree well with the dc resistances R_{dc} (impedance value when $f \to 0$) given by the impedance measurements [Eq. (25) and Eq. (44) for the constant temperature difference and constant heat power input, respectively], as shown in Table 4, where deviations between both resistances are below 2%. This is expected, since all the *I-V* curves (except the fast curve) are recorded under steady state condition, which is reached in the impedance measurements when $f \to 0$. This fact, allows knowing the different contributions to $R_{I\text{-}V}$ from the impedance measurements, as shown in Table 4. This is highly interesting, since the maximum power output of TE devices is given by $P_{max} = V_{oc}^2/(4R_{I\text{-}V})$, being V_{oc} the open-circuit voltage [3]. Since V_{oc} is the same for all the systems under 10 K temperature difference (see Fig. 11), the maximum power output strongly depends on the value of $R_{I\text{-}V}$, whose contributions can be determined by impedance measurements using the analysis presented here.

For the case under constant heat power input, only two contributions govern $R_{I\text{-}V}$ [see Eq. (44)]: R_{Ω} and R_{TE}. Since both resistances add together and their values do not differ much (1.241 and 0.949 Ω, respectively) they have similar contributions and it is important to reduce both of them. This can be achieved by decreasing the electrical conductivity and the thermal conductivity of the legs. If the latter is produced, it will increase V_{oc} as well, which is also desired to enhance P_{max}.

For the case under constant temperature difference, $R_{I\text{-}V}$ has a larger number of contributions [see Eq. (25)]: R_{Ω}, R_{TE}, R_{TC1}, R_M, R_{TC2}, $R_{S/C}$, and R_C. All of them represent the influence of the thermal contact resistances and the thermal conductivities of the metallic strips and external ceramic layers, apart from the TE properties of the legs. As it can be seen from Table 4, the most significant contributions come from R_{Ω} and R_{TE}, (as in the constant heat power input case) with the addition of R_{TC}. This highlights the importance of reducing as much as possible

the thermal contact resistance between the module and the heat exchangers (or heat source/heat sink). Moreover, this reduction will also lead to a significant increase of V_{oc}. Since R_{TC} connects in parallel with R_{TE}, a more reduced $R_{I\text{-}V}$ will typically occur for the constant temperature difference case. It should be noticed that a similar analysis was performed by us solving the heat equation under steady-state conditions in a previous article [26], although the internal thermal contact resistances (r_{TC1} and r_{TC2}) were not considered in that study.

When determining R_Ω and R_{TE}, which define the dimensionless figure of merit of the TE module ($zT = R_{TE}/R_\Omega$), both methods, an impedance spectroscopy measurement in suspended conditions and two *I-V* curves (one at a very high scan rate and another under constant heat power input) provide the same information. Two impedance spectroscopy measurements (one in suspended conditions) or an *I-V* curve is also enough to determine P_{max} in both cases (constant temperature difference and constant heat power input). However, if the aim is to determine r_{TC}, the use of the three *I-V* curves requires de assumptions of $r_{TC1} = 0$ and $r_{TC2} = 0$, making this method less accurate than two impedance measurements. Furthermore, impedance spectroscopy measurements can be used to determine properties of the TE module (e.g. r_{TC1}).

The fast *I-V* curve of Fig. 11, which was recorded at a very high scan rate, shows a 1.264 Ω slope value, which agrees well with all the R_Ω values in Table 4 (1.8% deviation). This occurs since the very high scan rate used does not allow the temperature difference to be established and the voltage drop is only given by IR_Ω ($S\Delta T = 0$). Finally, it can be seen that the $R_{I\text{-}V}$ values of the system under constant heat power (2.177 Ω) and the suspended device (2.226 Ω) are similar (2.2% deviation), as expected from the impedance analysis, since both $R_{I\text{-}V}$ values have the same contributions (R_Ω and R_{TE}). Hence, an *I-V* curve of a suspended device (or an impedance measurement) can be used to determine the power output of the system under constant heat power input (if S is known). It should be noted that for this to hold, also the assumptions adopted in our analysis should be fulfilled (e.g. adiabatic conditions).

5. Conclusions

This article analyses in detail the impedance response of TE modules under energy harvesting operation when a small temperature difference is present. The study covers the two most common cases in applications (constant temperature difference and constant heat power input). First, the theoretical models (equivalent circuits) were developed in both cases by solving the heat equation in the frequency domain under adiabatic conditions and considering all the main thermal phenomena occurring in the system, such as the thermal contact resistances between the TE module and the heat source and the heat sink, the internal thermal contact resistances (TE legs/metallic strips and metallic strips/external ceramic layers), the spreading-constriction effects, and the thermal influence of TE legs, metallic strips and ceramic layers. Then, the impedance response of a commercial bismuth telluride module was measured in the two cases under study, including measurements at different current-voltage points along the current-voltage curve, showing large differences between both scenarios. At the different points of the current-voltage curve, only significant differences were observed in the impedance spectra for the constant heat power input case, due to the variations of the ohmic resistance of the device with the average temperature. The developed equivalent circuits (provided as a MATLAB code) were used to successfully fit the experimental data and provided key parameters of the module, such as the thermal contact resistance between the TE device and the heat exchangers (heat source and heat sink), and the thermal contact resistance between the TE legs and the metallic strips.

On the other hand, it was found that the dc resistance obtained from the impedance response (when frequency tends to zero), matches with the slope of the current-voltage curve. In fact, the different contributions to this slope, which governs the power output, can be extracted from the impedance measurements. For the constant temperature difference case, only the ohmic and TE resistances contribute to the slope. However, under constant heat power input conditions, a larger number of additional contributions occur, coming from the influence of the thermal contact resistances and the thermal conductivities of the metallic strips and external ceramic layers. From all these additional contributions, it was identified that the influence of the thermal contact resistance between the device and the heat source heat sink was the most relevant. The new equivalent circuits developed allows the use of impedance for the characterization of TE devices under operating conditions (small temperature differences), which can determine key parameters of the device and the system. Also, all the analysis performed provides new insights to better understand the performance of TE modules and the contributions to the power output in different conditions of operation.

Nomenclature

TE	thermoelectric
I	current (A)
I_{ac}	current amplitude of an ac signal (A)
I_{dc}	current value around the oscillation of an ac signal is produced (A)
V	voltage (V)
V_{ac}	voltage amplitude of an ac signal (V)
V_{dc}	voltage value around which the oscillation of an ac signal is produced (V)
Z	Impedance (Ω)
$\|Z\|$	module of the impedance (Ω)
ϕ	phase angle (rad)
Z'	real impedance (Ω)
Z''	imaginary impedance (Ω)
N	number of couples of a thermoelectric device
A	area of the thermoelectric legs (m^2)
L	length of the thermoelectric elements (m)
η_M	ratio between area of all thermoelectric legs and all metallic strips
L_M	length of the metallic strips (m)
η	thermoelectric module filling factor, ratio area legs/area ceramics
L_C	length of the ceramic contacts (m)
r_{TC}	thermal contact resistivity between thermoelectric module and heat exchangers (m^2KW^{-1})
r_{TC1}	thermal contact resistivity between thermoelectric legs and metallic strips (m^2KW^{-1})
r_{TC2}	thermal contact resistivity between metallic strips and ceramics (m^2KW^{-1})
S	Seebeck coefficient (V/K)
σ	electrical conductivity (S/m)
λ_{TE}	thermal conductivity of the thermoelectric legs ($Wm^{-1}\ K^{-1}$)
α_{TE}	thermal diffusivity of the thermoelectric legs (m^2/s)
ω_{TE}	characteristic frequency of heat diffusion in the thermoelectric legs (rad/s)
λ_M	thermal conductivity of the metallic strips ($Wm^{-1}\ K^{-1}$)
α_M	thermal diffusivity of the metallic strips (m^2/s)
ω_M	characteristic frequency of heat diffusion in the metallic strips (rad/s)
λ_C	thermal conductivity of the ceramic layers ($Wm^{-1}\ K^{-1}$)
α_C	thermal diffusivity of the ceramics (m^2/s)
ω_C	characteristic frequency of heat diffusion in the ceramics (rad/s)
T	Temperature (K)
ΔT	temperature difference (K)
$T_{initial}$	initial temperature (K)
T_H	hot side temperature (K)
T_C	cold side temperature (K)
T_M	average temperature (K)
L_p	Inductance (H)

j	imaginary number
f	Frequency (Hz)
ω	angular frequency (rad/s)
R_Ω	total ohmic resistance (Ω)
θ_x	complex temperature increase at location x (Ks)
ϕ_x	complex heat flux at location x (Ws)
R	resistor (Ω)
C	capacitor (F)
Z_{WCT}	constant-temperature Warburg (Ω)
Z_{Wa}	adiabatic Warburg (Ω)
$z_{s/c}$	spreading-constriction impedance (m^2KW^{-1})
$r_{s/c}$	spreading-constriction resistivity (m^2KW^{-1})
Z_{So}	impedance of the heat source side (Ω)
Z_{Si}	impedance of the heat sink side (Ω)
L_{So}	length of the heat source (m)
λ_{So}	thermal conductivity of the heat source ($Wm^{-1}\ K^{-1}$)
α_{So}	thermal diffusivity of the heat source (m^2/s)
ω_{So}	characteristic frequency of heat diffusion of the heat source (rad/s)
R_{dc}	dc resistance (Ω)
V_{oc}	open-circuit voltage (V)
$R_{I\text{-}V}$	resistance (slope) of an *I-V* curve (Ω)
P_{max}	maximum power output of the thermoelectric device (W)
zT	dimensionless figure of merit

CRediT authorship contribution statement

Braulio Beltrán-Pitarch: Writing – original draft, Validation, Resources, Investigation, Funding acquisition, Formal analysis, Data curation, Conceptualization. **Francisco Vidan:** Validation, Data curation. **Marc Carbó:** Validation, Data curation. **Jorge García-Cañadas:** Writing – original draft, Validation, Supervision, Resources, Methodology, Investigation, Funding acquisition, Formal analysis, Data curation, Conceptualization.

Declaration of competing interest

The authors declare the following financial interests/personal relationships which may be considered as potential competing interests:

Jorge Garcia-Canadas reports financial support was provided by Spanish Agencia Estatal de Investigación and Universitat Jaume I. Braulio Beltran-Pitarch reports financial support was provided by Generalitat Valenciana and the European Social Fund. If there are other authors, they declare that they have no known competing financial interests or personal relationships that could have appeared to influence the work reported in this paper.

Data availability

Datasets related to this article can be obtained at Zenodo repository.

Acknowledgments

The authors acknowledge financial support from the Spanish Agencia Estatal de Investigación under the Ramón y Cajal Program (RYC-2013-13970), from the Generalitat Valenciana and the European Social Fund under the ACIF program (ACIF/2018/233) and BEFPI program (BEFPI/2019/030), from the Universitat Jaume I under the project UJI-A2016-08, and the technical support of Raquel Oliver Valls and José Ortega Herreros.

Appendix A. Supplementary data

Supplementary data to this article can be found online at https://doi.org/10.1016/j.apenergy.2024.123104.

References

[1] Rowe DM. Handbook on Thermoelectrics – Macro to Nano. CRC Press; 2006.
[2] Champier D. Thermoelectric generators: a review of applications. Energ Conver Manage 2017;140:167–81. https://doi.org/10.1016/j.enconman.2017.02.070.
[3] García-Cañadas J. Chapter 7. Thermoelectric modules: power output, efficiency, and characterization. In: Thermoelectr. Energy convers. Basic concepts device Appl. Wiley-VCH Verlag GmbH & Co. KGaA; 2017. p. 127–46. https://doi.org/10.1002/9783527698110.ch7.
[4] Lazanas AC, Prodromidis MI. Electrochemical Impedance Spectroscopy—A Tutorial. ACS Meas Sci Au 2023;3:162–93. https://doi.org/10.1021/ACSMEASURESCIAU.2C00070/SUPPL_FILE/TG2C00070_SI_001.ZIP.
[5] Barsoukov E, Macdonald JR, editors. Impedance spectroscopy: theory, experiment, and applications. Hoboken, NJ, USA: John Wiley & Sons, Inc.; 2018. https://doi.org/10.1002/9781119381860.
[6] Levi MD, Aurbach D. Simultaneous measurements and modeling of the electrochemical impedance and the cyclic voltammetric characteristics of graphite electrodes doped with lithium. J Phys Chem B 1997;101:4630–40. https://doi.org/10.1021/jp9701909.
[7] Fabregat-Santiago F, Garcia-Belmonte G, Mora-Sero I, Bisquert J. Characterization of nanostructured hybrid and organic solar cells by impedance spectroscopy. Phys Chem Chem Phys 2011;13:9083–118. https://doi.org/10.1039/c0cp02249g.
[8] Yuan XZ, Wang HJ, Sun JC, Zhang JJ. AC impedance technique in PEM fuel cell diagnosis - A review. Int J Hydrogen Energy 2007;32:4365–80. https://doi.org/10.1016/j.ijhydene.2007.05.036.
[9] Bisquert J, Fabregat-Santiago F. Impedance spectroscopy: a general introduction and application to dye-sensitized solar cells. In: Kalyanasundaram K, editor. Dye. Sol. Cells. EPFL Press; 2010. p. 457.
[10] Downey AD, Hogan TP, Cook B. Characterization of thermoelectric elements and devices by impedance spectroscopy. Rev Sci Instrum 2007;78:93904. https://doi.org/10.1063/1.2775432.
[11] De Marchi A, Giaretto V. An accurate new method to measure the dimensionless figure of merit of thermoelectric devices based on the complex impedance porcupine diagram. Rev Sci Instrum 2011;82:104904. https://doi.org/10.1063/1.3656074.
[12] García-Cañadas J, Min G. Impedance spectroscopy models for the complete characterization of thermoelectric materials. J Appl Phys 2014;116:174510. https://doi.org/10.1063/1.4901213.
[13] Beltrán-Pitarch B, García-Cañadas J. Influence of convection at outer ceramic surfaces on the characterization of thermoelectric modules by impedance spectroscopy. J Appl Phys 2018;123:084505. https://doi.org/10.1063/1.5019881.
[14] Mesalam R, Williams HR, Ambrosi RM, García-Cañadas J, Stephenson K. Towards a comprehensive model for characterising and assessing thermoelectric modules by impedance spectroscopy. Appl Energy 2018;226:1208–18. https://doi.org/10.1016/j.apenergy.2018.05.041.
[15] Yoo CY, Yeon C, Jin Y, Kim Y, Song J, Yoon H, et al. Determination of the thermoelectric properties of a skutterudite-based device at practical operating temperatures by impedance spectroscopy. Appl Energy 2019;251:113341. https://doi.org/10.1016/j.apenergy.2019.113341.
[16] Thiébaut E, Pesty F, Goupil C, Guegan G, Lecoeur P. Non-linear impedance spectroscopy for complete thermoelectric characterization: beyond the zT estimation. J Appl Phys 2018;124:235106. https://doi.org/10.1063/1.5063419.
[17] Beltrán-Pitarch B, Maassen J, García-Cañadas J. Comprehensive impedance spectroscopy equivalent circuit of a thermoelectric device which includes the internal thermal contact resistances. Appl Energy 2021:299. https://doi.org/10.1016/j.apenergy.2021.117287.
[18] Beltrán-Pitarch B, García-Cañadas J. Impedance spectroscopy analysis of thermoelectric modules fabricated with metallic outer external layers. ACS Appl Electron Mater 2021;3:4803–8. https://doi.org/10.1021/acsaelm.1c00670.
[19] Beltrán-Pitarch B, Vidan F, García-Cañadas J. Characterization of thermal contacts between heat exchangers and a thermoelectric module by impedance spectroscopy. Appl Therm Eng 2020;165:114361. https://doi.org/10.1016/j.applthermaleng.2019.114361.
[20] Apertet Y, Ouerdane H. Small-signal model for frequency analysis of thermoelectric systems. Energ Conver Manage 2017;149:564–9. https://doi.org/10.1016/j.enconman.2017.07.061.
[21] Boldrini S, Ferrario A, Miozzo A. Investigation of pulsed thermoelectric performance by impedance spectroscopy. J Electron Mater 2019;48:1805–11. https://doi.org/10.1007/s11664-018-06922-9.
[22] Lu C-T, Hsueh K-L, Li W-J, Liu C-M. (Invited) the electrochemical impedance spectra of BiTe thermoelectric device. ECS Trans 2017;80:89–102. https://doi.org/10.1149/08005.0089ecst.
[23] Aljaghtham M, Song G, García-Cañadas J, Beltrán-Pitarch B. Prismatic spreading-constriction expression for the improvement of impedance spectroscopy models and a more accurate determination of the internal thermal contact resistances of thermoelectric modules. ACS Appl Electron Mater 2023;5:3373–7. https://doi.org/10.1021/acsaelm.3c00389.
[24] Maillet D. Thermal quadrupoles : Solving the heat equation through integral transforms. Wiley; 2000.
[25] Pailhes J, Pradere C, Battaglia JL, Toutain J, Kusiak A, Aregba AW, et al. Thermal quadrupole method with internal heat sources. Int J Therm Sci 2012;53:49–55. https://doi.org/10.1016/j.ijthermalsci.2011.10.005.
[26] Beltrán-Pitarch B, Vidan F, García-Cañadas J. Thermal contact resistance evaluation of a thermoelectric system by means of three I-V curves. Int J Heat Mass Transf 2021;173:121247. https://doi.org/10.1016/j.ijheatmasstransfer.2021.121247.